



UvA-DARE (Digital Academic Repository)

The inner circumstellar dust of the red supergiant Antares as seen with VLT/SPHERE/ZIMPOL

Cannon, E.; Montargès, M.; de Koter, A.; Decin, L.; Min, M.; Lagadec, E.; Kervella, P.; Sundqvist, J.O.; Sana, H.

DOI

[10.1093/mnras/stab018](https://doi.org/10.1093/mnras/stab018)

Publication date

2021

Document Version

Final published version

Published in

Monthly Notices of the Royal Astronomical Society

[Link to publication](#)

Citation for published version (APA):

Cannon, E., Montargès, M., de Koter, A., Decin, L., Min, M., Lagadec, E., Kervella, P., Sundqvist, J. O., & Sana, H. (2021). The inner circumstellar dust of the red supergiant Antares as seen with VLT/SPHERE/ZIMPOL. *Monthly Notices of the Royal Astronomical Society*, 502(1), 369-382. <https://doi.org/10.1093/mnras/stab018>

General rights

It is not permitted to download or to forward/distribute the text or part of it without the consent of the author(s) and/or copyright holder(s), other than for strictly personal, individual use, unless the work is under an open content license (like Creative Commons).

Disclaimer/Complaints regulations

If you believe that digital publication of certain material infringes any of your rights or (privacy) interests, please let the Library know, stating your reasons. In case of a legitimate complaint, the Library will make the material inaccessible and/or remove it from the website. Please Ask the Library: <https://uba.uva.nl/en/contact>, or a letter to: Library of the University of Amsterdam, Secretariat, Singel 425, 1012 WP Amsterdam, The Netherlands. You will be contacted as soon as possible.

UvA-DARE is a service provided by the library of the University of Amsterdam (<https://dare.uva.nl>)

The inner circumstellar dust of the red supergiant Antares as seen with VLT/SPHERE/ZIMPOL

E. Cannon¹,¹★ M. Montargès¹,¹ A. de Koter^{1,2}, L. Decin^{1,3}, M. Min^{2,4}, E. Lagadec⁵, P. Kervella⁶, J. O. Sundqvist¹ and H. Sana¹

¹*Institute of Astronomy, KU Leuven, Celestijnenlaan 200D B2401, B-3001 Leuven, Belgium*

²*Anton Pannekoek Institute of Astronomy, University of Amsterdam, Science Park 904, NL-1098 XH Amsterdam, the Netherlands*

³*School of Chemistry, University of Leeds, Leeds LS2 9JT, UK*

⁴*SRON Netherlands Institute for Space Research, Sorbonnelaan 2, NL-3584 CA Utrecht, the Netherlands*

⁵*Laboratoire Lagrange, UNSA, CNRS, Obs. de la Cote d'Azur, Bd de l'Observatoire, F-06304 Nice Cedex 4, France*

⁶*LESIA, Observatoire de Paris, Université PSL, CNRS, Sorbonne Université, Université de Paris, 5 Place Jules Janssen, F-92195 Meudon, France*

Accepted 2020 December 22. Received 2020 December 22; in original form 2020 July 30

ABSTRACT

The processes by which red supergiants lose mass are not fully understood thus far and their mass-loss rates lack theoretical constraints. The ambient surroundings of the nearby M0.5 Iab star Antares offer an ideal environment to obtain detailed empirical information on the outflow properties at its onset, and hence indirectly, on the mode(s) of mass-loss. We present and analyse optical VLT/SPHERE/ZIMPOL polarimetric imaging with angular resolution down to 23 milliarcsec, sufficient to spatially resolve both the stellar disc and its direct surroundings. We detect a conspicuous feature in polarized intensity that we identify as a clump containing dust, which we characterize through 3D radiative transfer modelling. The clump is positioned behind the plane of the sky, therefore has been released from the backside of the star, and its inner edge is only 0.3 stellar radii above the surface. The current dust mass in the clump is $1.3^{+0.2}_{-1.0} \times 10^{-8} M_{\odot}$, though its proximity to the star implies that dust nucleation is probably still ongoing. The ejection of clumps of gas and dust makes a non-negligible contribution to the total mass lost from the star that could possibly be linked to localized surface activity such as convective motions or non-radial pulsations.

Key words: radiative transfer – techniques: polarimetric – stars: imaging – stars: individual: Antares – stars: mass-loss – supergiants.

1 INTRODUCTION

During their red supergiant (RSG) phase of evolution, massive stars ($8 < M < 30 M_{\odot}$; Ekström et al. 2012) experience an important mass-loss (10^{-6} – $10^{-4} M_{\odot} \text{ yr}^{-1}$; van Loon 2006; De Beck et al. 2010) which strongly impacts their final mass, hence the properties of the supernova (SN) progenitor and of the compact remnant that is left behind. Material that is lost in the stellar wind, together with that ejected in the final core collapse, contributes to the chemical enrichment of the interstellar medium. The mass-loss properties of RSGs are however poorly constrained, and little is known about the mechanism(s) driving material from the surface. Without this knowledge, it is difficult to build reliable theoretical models to predict mass-loss rates and therefore difficult to deduce the initial mass of SN IIP and IIL progenitors. This situation is problematic, not only from the perspective of understanding massive star evolution and the role of RSG in stellar feedback, but also with respect to fathoming the so-called Red Supergiant Problem (i.e. the lack of detections of progenitors with initial mass $> 17 M_{\odot}$; Smartt 2009), which may be connected to an underestimated RSG mass-loss (Ekström et al. 2012; Georgy 2012).

Several mechanisms have been proposed that could contribute to RSG mass-loss. Most invoke a stellar wind driven by radiation pressure on dust grains, similar to the mechanism proposed for asymptotic giant branch (AGB) stars (Höfner 2008; Höfner et al. 2016). However, it is doubtful whether the prevailing thermodynamic conditions to grow grains in the first place are comparable for AGB and RSG stars (Höfner & Freytag 2019). Radiation pressure exerted on spectral lines of molecular species may be an alternative, though at the present time it is unclear whether this provides sufficient driving in the onset region of the flow (Bennett 2010). The possibility of an Alfvén wave-driven wind has also been explored by Airapetian et al. (2000) and a wave-driven mass-loss model for Betelgeuse can be seen in Hartmann & Avrett (1984). A further alternative is that the mass-loss trigger is linked to surface activity, where pulsations and large convective cells upwelling from the sub-photosphere may lower the effective gravity allowing radiation pressure to launch material (Josselin & Plez 2007).

Observations of Antares, one of the closest RSGs, by Montargès et al. (2017) with the VLT/PIONIER instrument revealed that convective cells of various sizes cover the stellar surface, confirming early indications of the presence of such structures by Tuthill, Haniff & Baldwin (1997) who detected variable hotspots on the stellar surface and Richichi & Lisi (1990) who suspected an asymmetric brightness profile. Above the surface (out to 1.7

* E-mail: emily.cannon@kuleuven.be

Table 1. Log of SPHERE/ZIMPOL observations of Antares and reference star ϵ Sco.

Star	Time UT 2015-06-25	Filter	ND	θ (ar- cmin)	DIT(s) \times NDIT	AM	θ_{PSF} (mas)
Antares	01:29:08	CntH α	ND_2	0.61	1.2×20	1.069	–
		NH α	ND_2	0.61	1.2×20	1.069	–
	01:55:12	BH α	ND_2	0.61	1.2×20	1.034	–
		TiO	ND_2	0.61	1.2×20	1.034	–
	02:27:17	V	ND_1	0.66	1.2×20	1.009	–
KI		ND_1	0.66	1.2×20	1.009	–	
ϵ Sco	00:40:42	CntH α	ND_1	0.70	1.2×20	1.236	26
		NH α	ND_1	0.70	1.2×20	1.236	27
	00:53:29	BH α	ND_1	0.83	1.2×20	1.197	25
		TiO	ND_1	0.83	1.2×20	1.197	24
	01:05:17	V	ND_1	0.61	1.2×20	1.166	30
		KI	ND_1	0.61	1.2×20	1.166	25

Note. ND indicates which neutral density filter has been used, θ is the visible seeing, AM gives the airmass, and θ_{PSF} is the FWHM of the PSF images. DIT gives the integration time of each frame and NDIT is the number of integrations. The filter pairs grouped together in time were observed simultaneously using the two arms of the detector. The characteristics of the filters are given in Table 2.

stellar radii), turbulent motion of large clumps of gas were observed using VLT/AMBER (Ohnaka, Weigelt & Hofmann 2017). Moving further away from the star, Ohnaka (2014) detected large clumps containing dust within 40–96 R_* with VLT/VISIR, upholding first indications for the presence of dusty clumps by Marsh et al. (2001). To investigate whether there is a link between surface convection and these clumps in the ambient environment, observations of the innermost circumstellar environment are needed. This is made possible by the high-spatial resolution polarimetry capabilities of SPHERE/ZIMPOL at ESO’s VLT observatory in Paranal, Chile. This instrument, with angular resolution up to 23 mas is capable of resolving the surfaces of the two closest RSGs, Antares and Betelgeuse, allowing the dust in the inner wind to be probed in detail. Betelgeuse has previously been observed using this instrument by Kervella et al. (2016).

In this paper, we present SPHERE/ZIMPOL observations of the RSG Antares along with 3D radiative transfer modelling of its ambient surroundings in order to characterize the spatial distribution and amount of dust near the surface. The observations and data reduction are described in Section 2 followed by their analysis in Section 3. The model set-up and results are described in Section 4. We discuss our findings in Section 5 and end with a summary and conclusions in Section 6.

2 OBSERVATIONS AND DATA REDUCTION

Antares (α Sco A, HD 148478, HD 6134) is an M0.5 Iab (Corbally 1984) RSG star at a distance of 170_{-25}^{+29} pc (van Leeuwen 2007). As such, it is one of the largest and visually brightest stars in the sky. It has an angular diameter of 37.89 ± 0.10 mas at the H $^-$ opacity minimum at $1.61 \mu\text{m}$ (Montargès et al. 2017) and 37.38 ± 0.06 mas in the K-band continuum (Ohnaka et al. 2013). Antares is known to have a companion, the B2.5 V star α Sco B, at a 2.73 arcsec angular separation (in 2006), approximately 224 au behind the supergiant (Reimers et al. 2008).

Observations of Antares, and a corresponding point spread function (PSF) calibrator star, ϵ Sco, were taken on 2015 June 25. These observations were carried out using SPHERE/ZIMPOL (Beuzit et al. 2019), a high-resolution adaptive optics imaging polarimeter, at ESO’s Very Large Telescope (VLT). Antares and its calibrator were observed in six filters in the visible. The log of the observations

Table 2. Filter characteristics and calculated photometry of Antares.

Filter	λ (nm)	$\Delta\lambda$ (nm)	Flux $10^{-8} \text{ W m}^{-2} \mu\text{m}^{-1}$
V	554	80.6	$1.555_{-0.561}^{+0.642}$
CntH α	644.9	4.1	$2.894_{-0.844}^{+1.003}$
BH α	655.6	5.5	$2.556_{-0.852}^{+0.722}$
NH α	656.34	0.97	$2.964_{-0.831}^{+0.968}$
TiO	716.8	19.7	$2.545_{-0.689}^{+0.794}$
KI	770.2	21.2	$3.679_{-0.922}^{+1.053}$

Note. $\Delta\lambda$ indicates the FWHM of the filter.

is presented in Table 1. The filter characteristics are given in Table 2.

Due to atmospheric or instrumental conditions, the adaptive optics loop of the instrument frequently opened during the observations. To eliminate the corrupted frames, we performed a selection on the raw data before executing the instrument pipeline. We determined the average of the flux of each frame in a circular area centred on the maximum. For each couple target/filter, we rejected the frames for which the mean central flux was below a specific threshold. The threshold in each case is then defined by 0.5, 2, or 5 standard deviations from the mean depending on the dispersion of the flux points for the individual case. Next, the raw data were processed using the ESO reflex data reduction pipeline v0.24.0 (Freudling et al. 2013). From this data, we then computed the total intensity, the degree of linear polarization (DoLP), the polarized intensity, and the polarization position angle as described by Kervella et al. (2015). The linear polarized intensity (Fig. 1) is defined by $\sqrt{Q^2 + U^2}$, where Q and U are Stokes parameters. The DoLP, being the polarized intensity divided by the intensity, gives us the fraction of the light that is linearly polarized. The observations were centred by fitting a Gaussian function to the intensity images to locate the centre of the star. The total intensity images of Antares were deconvolved using the Lucy–Richardson deconvolution algorithm implemented in IRAF (Lucy 1974) using the intensity images of ϵ Sco as the PSF (Fig. 2). The number of iterations needed in this process was judged by matching the measured angular diameter of the star to that of the deconvolved image. Beyond five iterations no further changes were measured in the full width at half-maximum (FWHM) of the intensity profiles.

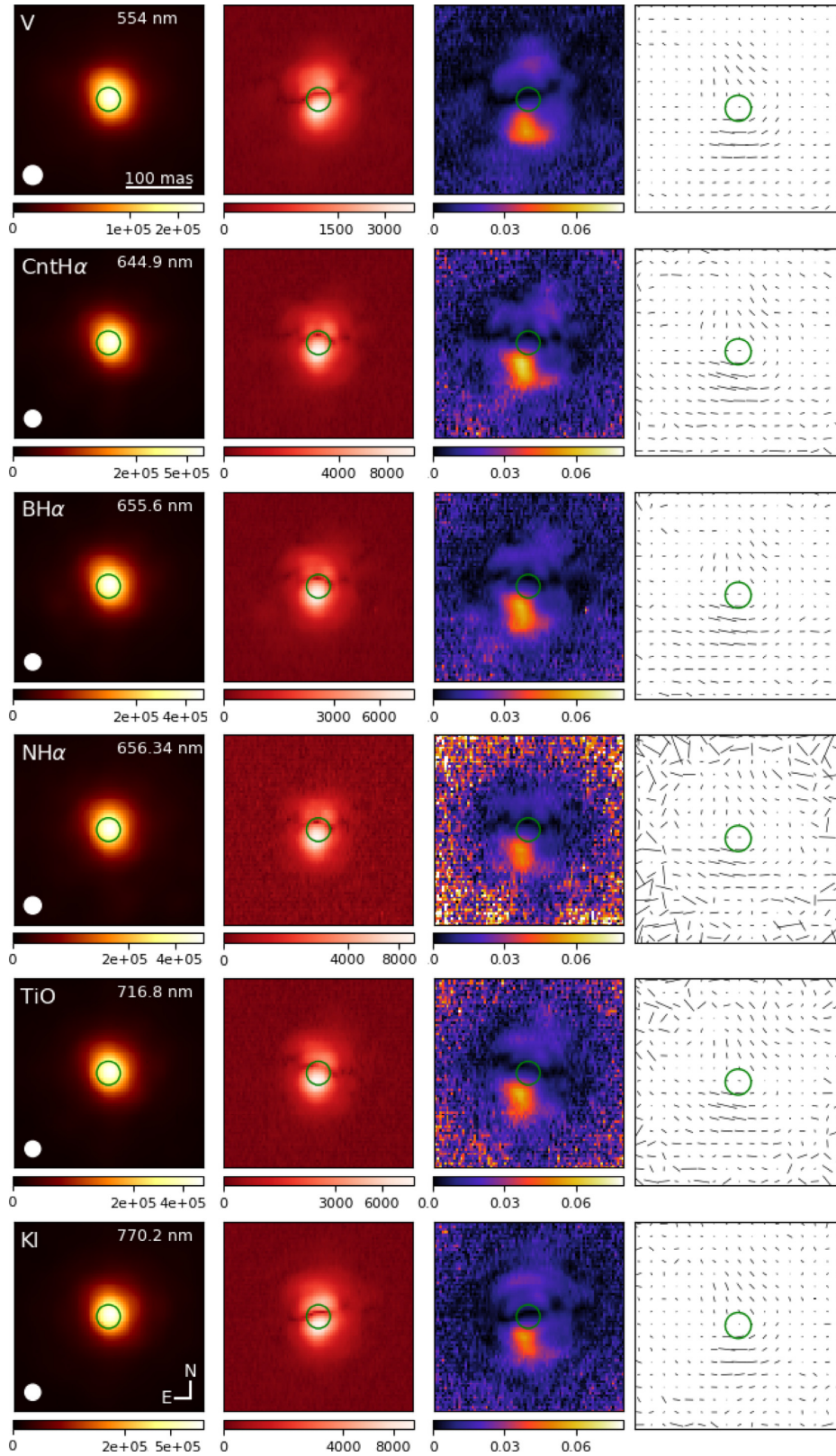


Figure 1. First column: Intensity images ($\text{W m}^{-2} \mu\text{m}^{-1} \text{sr}^{-1}$) of Antares, in square root scale. The filled white circle indicates the beam size and the green circle indicates the size of the photosphere (Ohnaka et al. 2013). Second column: Polarized flux ($\text{W m}^{-2} \mu\text{m}^{-1} \text{sr}^{-1}$), in square root scale. Third column: DoLP in linear scale spanning 0–8 per cent. Last column: Angle of the polarization vector. The magnitude of the vector is scaled to the strength of the DoLP at each point.

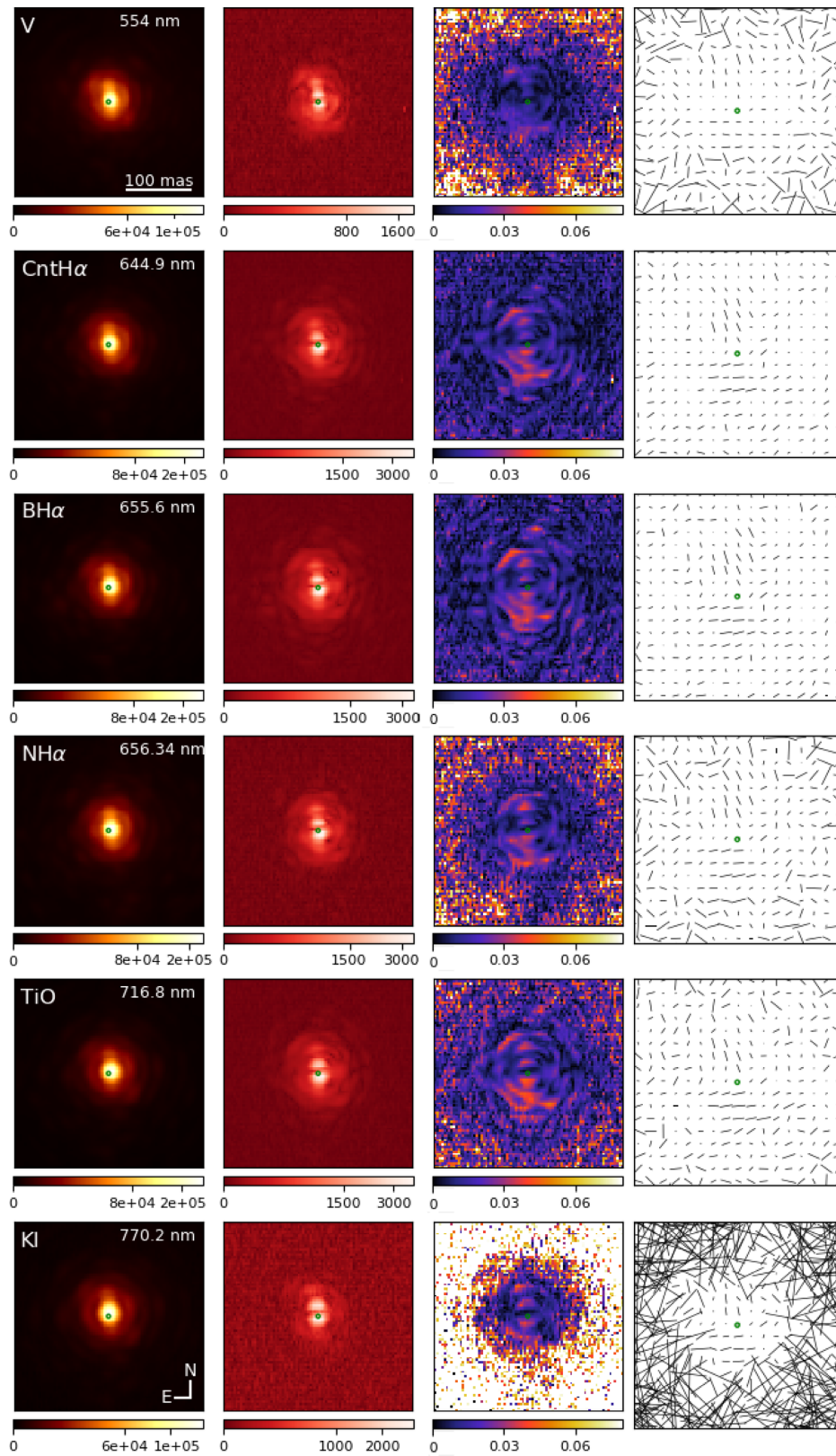


Figure 2. Same as Fig. 1 but for ϵ Sco.

The SPHERE/ZIMPOL pipeline products are not flux calibrated. In order to derive the observed flux in each filter for Antares, we first matched a stellar atmosphere model from Castelli & Kurucz (2003) to the calibrator star, ϵ Sco. As ϵ Sco is a K1III star (Gray et al. 2006), we selected a model with an effective temperature of 4500 K, $\log g = +2.50$ with solar metallicity in agreement with McWilliam (1990). We scaled this theoretical spectral energy distribution (SED) using the angular diameter of the star, 5.747 ± 0.008 mas (Richichi, Percheron & Davis 2009), and compared to existing photometry (Ducati 2002) to confirm the suitability of the model. The theoretical flux for each of the SPHERE filters that were observed was calculated by integrating over the SED after convolving with the SPHERE transmission filters. We determined the observed flux in the image by summing the intensity over a circular aperture of 184 mas centred on the star. The background flux was estimated using a ring, with inner and outer radii of 184 and 220 mas, respectively, and subtracted. From this, we obtained a conversion factor that was applied to the Antares data. The uncertainty estimation on the calibrated flux is dominated by that on the effective temperature of the calibrator star. This uncertainty is therefore set by the spacing of the stellar atmosphere model grid as this sampling is certainly larger than the uncertainty of the effective temperature leading to a conservative uncertainty estimate of ± 250 K. The flux calibrated intensity images of Antares are represented in Fig. 1 together with the polarimetric maps. The same for ϵ Sco is shown in Fig. 2. The deconvolved intensity images of Antares can be seen in Fig. 3.

3 DATA ANALYSIS

3.1 Intensity

Fig. 4 shows the flux obtained in each ZIMPOL filter we observed. As Antares is a semiregular variable, we also compared our flux with a measurement from the American Association of Variable Star Observers (AAVSO) in the V band (Fig. 4) taken within 24 h of our SPHERE observations and found our results to be in agreement. They are broadly consistent with previously measured photometry by Ducati (2002).

With a beam size (see Table 1) for each of the observations smaller than that of the projected surface size of the star, the stellar disc is resolved in all filters. Fitting a 2D Gaussian function to the deconvolved intensity images (Fig. 3) reveals that the visible photosphere departs from spherical symmetry in all filters giving eccentricities between 0.4 and 0.52 that could perhaps indicate that there is a temperature variation on the surface of the star.

3.2 Polarized flux

Significant signal can be seen in the polarized flux and DoLP across the six filters (see third column in Fig. 1). The DoLP that we see in each of the images is considerably higher than the polarization that is caused by the instrument itself, which is approximately 0.5 per cent (Beuzit et al. 2019).

There is a dark lane that runs through the centre of all polarization images which is non-physical and is due to a beam shift effect. This effect is introduced by the instrument mirrors and is further detailed by Schmid et al. (2018). Outside of the area plotted in Figs 1 and 2, the images are dominated by noise [causing the large polarization vectors at the edges of the images; for the corresponding root mean square (RMS) maps, see Fig. A1]. No significant stellar signal is seen in the DoLP of the calibrator star (Fig. 2), the signal present in

these images follows the diffraction rings caused by the telescopes mirror and is split East–West by the beam shift effect.

A large, conspicuous feature can be seen to the south of Antares in the DoLP in all filters. In the plane of the sky, the onset of the feature appears to be right at the stellar surface with a projected surface size greater than that of the star. This polarization could be caused by the scattering of the light by circumstellar dust grains or scattering off molecules or free electrons (Zubko & Laor 2000). The latter option seems unlikely given the low-ionization temperature associated with the radiation field from Antares. The polarization seen in the observations is consistent with the dust hypothesis as it is present throughout the entire wavelength range which would not be expected if the polarization was a result of light scattering off molecules within specific lines. The directions of the polarization vectors at the location of the feature are tangential to the stellar photosphere, as expected from the scattering of light from the central source by dust in the circumstellar environment. Henceforth, we refer to the feature as the clump.

4 MCMAX MODELLING

In order to determine if the dust hypothesis to explain the polarization signal around Antares is plausible and to characterize the dust causing the scattering, we run a radiative transfer model using MCMAX3D (Min et al. 2009), a 3D Monte Carlo radiative transfer code. MCMAX3D implements Mie scattering on a distribution of dust grains modelled as hollow spheres. The latter does not imply that the grains are truly hollow spheres; rather this assumption assures that the symmetrical nature of solid spherical particles, as in standard Mie theory, is broken (Min et al. 2004; Min, Hovenier & de Koter 2005). An ensemble of hollow spheres thus better represents the properties of a true distribution of non-spherically symmetric particles. The images of the Stokes vectors (I, Q, and U) are computed taking into account the diameter of the telescope mirror and can therefore be compared directly to the SPHERE observations. Through this modelling of our observations, we aim to provide constraints on the spatial distribution and total mass of the dust.

We focus the modelling on the conspicuous clump to the south of Antares that is seen in the DoLP. The polarization signal to the north of the star is several times fainter than that in the south and not well defined in all filters, for these reasons we concentrate our modelling efforts on the southern clump. We approximate the clump as a sphere of dust with a constant density as the number of resolution elements over the clump is a few. Therefore, we would have no diagnostic tools to constrain properties of a (spherical) density structure in the clump. The centre of the clump is placed at different (x, y, z) positions relative to the stellar centre, such that if we can constrain its 3D position we may link it to a surface release location assuming the clump is moving radially outwards. For clarity, z is the position along the line of sight (positive in the direction of the observer), y is the north–south axis (where north is positive), and x the east–west axis (where west is positive). The x coordinate of the clump centre is kept fixed based on the observations. Below, we discuss the assumptions regarding the composition and size of the dust particles. If we ignore the latter properties for now, our modelling space consists of four variables: z and y position, radius R_{clump} , and dust mass of the clump M_{clump} . To probe these dimensions, we have constructed a grid of models of varying step-size in each dimension. The ranges and step sizes of each of the four parameters are visualized in Fig. 5. We note here, first, that R_{clump} was varied between 1 and $5 R_*$, where $R_* = 680 R_{\odot}$ is the radius of Antares. Second, the parameter controlling the mass of the dust is sampled rather unevenly to ensure an unbiased density

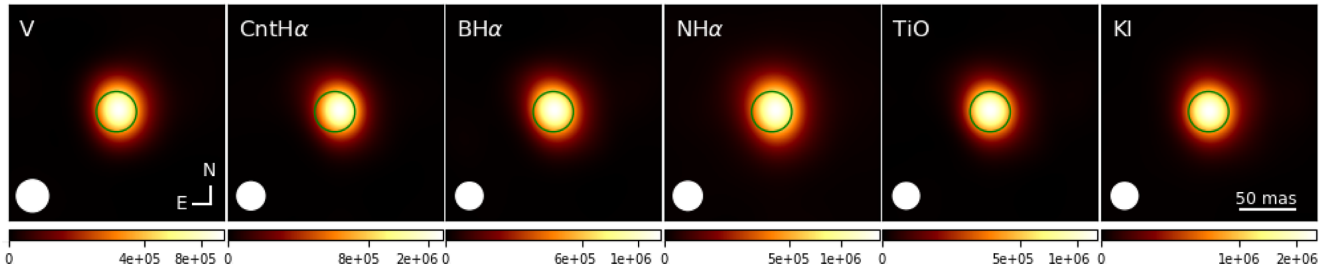


Figure 3. The deconvolved intensity images ($\text{W m}^{-2} \mu\text{m}^{-1} \text{sr}^{-1}$) of Antares in each filter, shown in square root scale. The photospheric size, measured by Ohnaka et al. (2013) in the near-infrared, is shown in green.

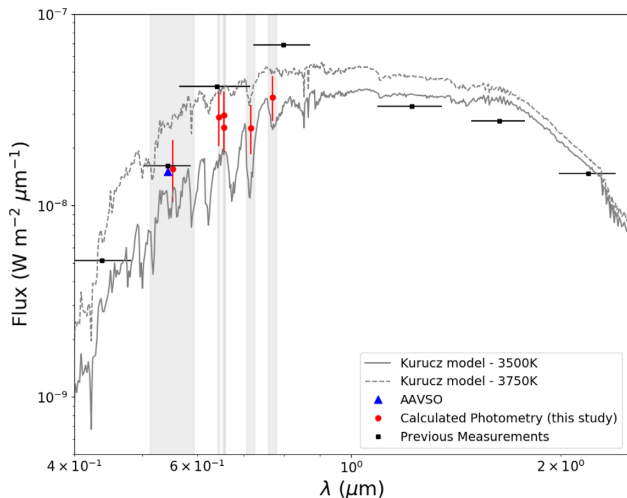


Figure 4. Antares photometry. A stellar atmosphere model from Castelli & Kurucz (2003) with $T_{\text{eff}} = 3500$ K, $\log g = 0$ and solar metallicity, scaled to the angular diameter of Antares and reddened is shown in grey. Similarly, a model with $T_{\text{eff}} = 3750$ K is shown by the dashed line. The grey shaded areas represent our six ZIMPOL filters (NH α and BH α overlap). The horizontal bars on the previously measured photometry by Ducati (2002) give the width of the Johnson bands. The blue triangle is a measurement in the V band from AAVSO that was taken on 26-06-2015 (one day apart from our observations).

sampling as the volume of the dust sphere varied. Third and finally, the y coordinate was allowed to vary as it was difficult to determine how far south the centre of the clump is in the observations as the models show that the DoLP signal is not constant through the large clump, i.e. the signal is concentrated in a smaller portion of the dust sphere (see also Section 5).

4.1 Parameters and assumptions

4.1.1 Stellar parameters

To determine the stellar energy distribution to use as input for the radiative transfer models, we first applied a reddening law to two stellar atmosphere models from Castelli & Kurucz (2003) with $T_{\text{eff}} = 3500$ and 3750 K, and surface gravity $g = 1 \text{ cm s}^{-1}$. We use $A_V = 0.43$ and $R_V = 3.1$ from Ohnaka et al. (2013) and follow the law described in Cardelli, Clayton & Mathis (1989). Both models are plotted in Fig. 4 and show that the photometry we retrieved from the SPHERE data falls between the two models. As Ohnaka et al. (2013) determine a T_{eff} of 3660 ± 120 K, this is unsurprising. A χ^2 test determines the model with $T_{\text{eff}} = 3500$ K to be the better fit so we proceed with a stellar atmosphere model at this temperature for the MCMAX3D

modelling input. A test between two radiative transfer models with $T_{\text{eff}} = 3500$ and 3750 K, showed no significant difference in the DoLP. The luminosity of $62\,500 L_{\odot}$ was set so that the angular diameter of the model star was consistent with previous interferometric measurements from Ohnaka et al. (2013) at a distance of 170 pc.

The star is modelled as a spherical object though both simulations and observations of RSGs indicate that this is not exactly the case due to their large convective cells. Similarly, the code assumes isotropic light emission. For the scope of this study, these assumptions are reasonable as we focus on the modelling of a large dust clump illuminated by a large fraction of the surface of the star.

4.1.2 Dust composition and grain size

Aronson, Bladh & Höfner (2017) report that the chemical composition of circumstellar dust grains cannot be reliably determined using observations in the visible regime alone but also need measurements in the near-IR. We therefore do not attempt to do so here. Verhoelst et al. (2009) review studies addressing this topic and provide an overview of likely dust constituents: aluminium oxide (Al_2O_3); melilite ($\text{Ca}_2\text{Al}_2\text{SiO}_7$); olivine ($\text{Mg}_{2x}\text{Fe}_{2-2x}\text{SiO}_4$; $0 \leq x \leq 1$); iron magnesium oxide (MgFeO); metallic iron (Fe), and carbon (C). Aluminium oxide is expected to condense early on in the condensation cycle (e.g. Tielens 1990). A study of dust precursors in AGB star winds by Boulanger et al. (2019) finds Al_2O_3 to be a potential first species to condense from the gas phase on the condition that the monomer $(\text{Al}_2\text{O}_3)_{n=1}$ forms. Depending on local density, cluster formation starts at temperatures as high as $1600\text{--}2200$ K the highest of all species trialled by them. As the dust in the observations appears close to the stellar surface and therefore at high temperatures, for this study we used dust composed of Al_2O_3 adopting the optical properties from Begemann et al. (1997) derived in the range $7.8\text{--}200 \mu\text{m}$. For shorter wavelengths, the optical constants are extrapolated following Bohren & Huffman (1998). This extrapolation implies that the alumina grains are almost transparent at optical wavelength, in line with findings by Koike et al. (1995). A study by Höfner et al. (2016) explores Al_2O_3 formation around M-type AGB stars. In this study, they show that Al_2O_3 forms closer to the star than silicates and may act as seed particles for the condensation of silicates further out.

Two other compositions were trialled, a mixture of MgSiO_3 + amorphous carbon, and the dust composition found by Verhoelst et al. (2009) comprising majorly of melilite with smaller amounts of olivine, alumina, and carbon. We found that the DoLP is not strongly sensitive to composition, though the best-fitting parameters (x , y , R_{dust} , M_{dust}) will differ somewhat from those derived using aluminium oxide. Specifically, these other compositions produce slightly less polarization. These differences are, however, so small that they do not

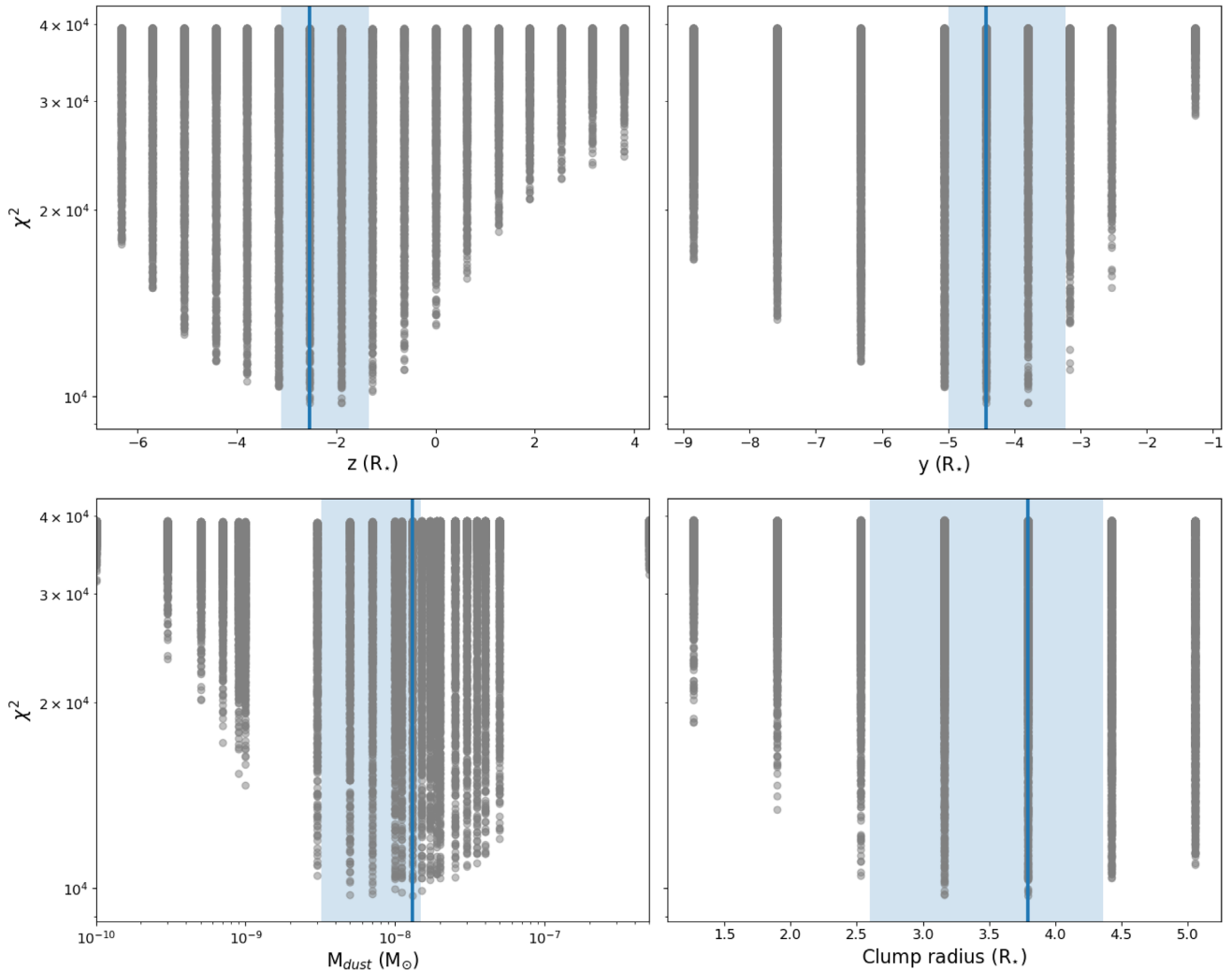


Figure 5. χ^2 values derived from the comparison of the DoLP from the ZIMPOL observations and MCMAX3D simulations against the four variables. Here, z is the line of sight and y is the North–South axis. The solid line indicates where the best-fitting model falls and the shaded region shows the confidence intervals.

impact our conclusions. We do point out that these alternative grains are more opaque than Al_2O_3 , therefore their temperatures are higher. We established that if the grain composition is actually a mixture of species – which is very likely – part of the volume of the best solution for our aluminium oxide only model would be too hot for these other grains to exist, either as thermally isolated species or as species in thermal contact. For the Verhoelst et al. (2009) mixture, this volume fraction is about 8 per cent (10 per cent when $T_{\text{eff}} = 3750$ K) if a condensation temperature of 1500 K is assumed, a result that has a modest impact on the assumption for the dust-to-gas ratio of the clump (see Section 5.1). One should note that this estimation does not take into account the presence of a warm chromosphere (see e.g. Harper, Brown & Lim 2001, and references therein) around an RSG such as Antares. Recently, O’Gorman et al. (2020) have shown that the interaction between the warm chromosphere at several thousand Kelvin and the cool gas which allows dust condensation in the same location is very complex: the detection of one or another is highly dependent on the wavelength used for the observations. It is likely that the warm gas is not dense and has a limited role on the dust condensation sequence. Therefore, as MCMAX3D cannot take this temperature profile into account, we do not include it in our models.

In conclusion: we expect the composition (in the bulk of the clump) to be a mixture typical for RSG outflows, however, we adopt the optical properties of aluminium oxide in our modelling to avoid partial dust condensation issues in the clump. Derived dust masses represent that of the actual dust mixture.

The DoLP is sensitive to the size distribution of the grain population; large grains producing less polarization relative to small grains in the wavelength range of our observations. Our observational data do not allow to place firm constraints on these properties, and we limit our investigation to assessing whether the wavelength dependence of the DoLP in the best-fitting model is consistent with our measurements (see Section 4.2). We follow Verhoelst et al. (2009) and adopt an MRN distribution of sizes described in Mathis, Rumpl & Nordsieck (1977), $n(a) \propto a^{-3.5}$, characteristic for interstellar particles, with sizes a in the range 0.01–1 μm . We prefer this approach over adopting a single particle size (e.g. van Loon et al. 2001; Beasor & Davies 2016) as likely stochastic processes play a role in dust formation and growth. Our adopted size distribution is shifted to slightly larger grains in comparison with Kochanek, Khan & Dai (2012) and Ohnaka (2014). Micron-sized grains in the circumstellar environment of Antares are reported in Snow et al. (1987) giving

Table 3. Summary of adopted stellar parameters and fitted clump parameters.

Parameter	Value	Confidence interval	Unit
T_{eff}	3500		K
g	1		cm s^{-2}
R_{\star}	680		R_{\odot}
x	-0.3		R_{\star}
y	-4.4	-5.0–-3.2	R_{\star}
z	-2.5	-3.1–-1.3	R_{\star}
d_{clump}	5.1	4.1–5.2	R_{\star}
ρ_{clump}	1.07	0.70–1.10	$10^{-18} \text{ g cm}^{-3}$
R_{clump}	3.8	2.6–4.4	R_{\star}
M_{clump}	1.3	0.3–1.5	$10^{-8} M_{\odot}$

Note. Where d_{clump} is the distance from the centre of the star to the centre of the clump.

weight to theoretical considerations of dust driving in cool star outflows that seem to favour fairly large grains (Höfner 2008).

4.2 Modelling results

To determine the best-fitting model to the observations, we used a χ^2 minimization technique. First, we compute χ^2 for each of our models using:

$$\chi^2 = \sum_{i=1}^n \frac{(O_i - E_i)^2}{\sigma_i^2}, \quad (1)$$

where O and E are the flux in pixel i for our observations and models, respectively, σ is the error in the observed data (see Fig. A1) and n is the total number of pixels in our cubes ($n = 33\,620$). In this case, we directly compared the DoLP image outputted by our models to the observed images in all filters by summing over the total number of pixels after cutting the images to a 300×300 mas field of view.

In order to calculate the confidence interval on the parameter ranges, we use the same method as outlined in Tramper et al. (2011) and Abdul-Masih et al. (2019). The χ^2 values from the grid were normalized such that the best-fitting model had a χ^2_{red} value of 1. From here the P-value was calculated, all models with a P-value higher than 0.05 (therefore within the 95 per cent confidence interval) are deemed acceptable models that are statistically indistinguishable from each other. It is from these models that we are taking our parameter ranges for the position, radius, and dust mass of the clump. Due to computational limitations, we had to limit the sampling rate. To account for this, we perform a linear interpolation to the upper P-value points to give a better estimate on the confidence interval on each parameter.

Fig. 5 shows the χ^2 distribution for our grid of models. For each of our variable parameters relatively clear minima can be seen in the χ^2 distribution. Table 3 shows the parameters of the best-fitting models from the grid using Al_2O_3 for the dust composition. As can be seen in Fig. 5, all of these models place the dust behind the plane of the star at close proximity to the photosphere. Table 3 shows that as the mass and radius of the dust clump display large confidence intervals, the dust density in the clump remains relatively constant for our best-fitting models.

Fig. 6 shows the intensity, polarized flux, and DoLP for the best-fitting model. A side-by-side comparison of the observations and best-fitting model can be seen in Fig. 7. At longer wavelengths, the DoLP diminishes relative to the observations. However, the fit remains within the uncertainties of the (polarized)-flux calibration (see Fig. 8).

5 DISCUSSION

5.1 Properties of the dusty clump

For our homogeneous spherical distribution of dust grains, the best fit to the DoLP images places the centre of the clump at $5.1 R_{\star}$ and yields a clump radius of $3.8 R_{\star}$. Fig. 9 provides a schematic of the geometry of the system. The clump is considerably larger than the star itself with the smaller clumps failing to produce as much polarization signal. The reason for this is the combined effect of the non-isotropic nature of scattering of light off of dust grains (which has a maximum polarization for 90° scattering angle) and the marginally optically thick nature of the clump at optical wavelengths. One therefore most prominently observes polarization from the part of the clump that is closest to the star.

The visual extinction in the V-band of a line of sight through the centre of the clump is about $A_V = 3.6$. A similar clump perfectly aligned in front of the stellar disc would have reduced the visual light flux by a large factor ($\simeq 35$). This could be an explanation of what has happened to Betelgeuse in 2019–2020, where a significant dimming was observed in visible light (photo release ESO/Montargès et al.¹; Levesque & Massey 2020). Given the dimensions of the clump, it fills 18 per cent of the total sky as seen from Antares, i.e. a minimum of about 5–6 such clump are needed to cover the entire surface.

Mauron & Josselin (2011) assume the gas-to-dust ratio in the circumstellar environment of RSGs to be $\psi = 200$ in the limit of full condensation of refractory metals. However, a general value of ψ for RSGs still remains highly uncertain. For aluminium oxide, the dust temperatures in the clump range from approximately 40 to 1000 K. In Section 4.1.2, we pointed out that about 8 per cent of the clump is, however, too close to the surface to allow silicate or carbon-based grains to survive. Assuming rapid formation (for time-scales refer to Boulanger et al. 2019) of these species once the local temperature drops below the condensation temperature as the clump moves away from the surface, we derive a mean gas-to-dust ratio in the clump using $1/\psi = 0.92/200 + 0.08/7000$, i.e. $\psi \simeq 215$, applying 7000 for the gas-to-dust ratio of fully condensed alumina in a solar abundance mixture (Asplund et al. 2009) and gas-to-dust ratio of 200 for the rest of the clump. Using a total mass of grains of $1.3 \times 10^{-8} M_{\odot}$, this implies a total mass of the clump of $\sim 2.8 \times 10^{-6} M_{\odot}$.

We lack velocity information for the conspicuous nearby dusty clump. Obtaining such kinematic information through resolved spectroscopy is crucially important for identifying the launching and/or driving mechanism of the clump and the time of ejection. Using a speculative velocity of 30 km s^{-1} (inspired from findings by Ohnaka 2014; see below), which is lower than the local escape velocity at $r = 5.11 R_{\star}$ of 43 km s^{-1} , the clump would have been ejected about 2 yr prior to our observations. Note that within this hypothesis, the clump would fall down on the star and sublimate, if the radiative pressure on the newly formed dust does not succeed in accelerating it further.

5.2 Dusty clumps further away from Antares

Ohnaka (2014) uses VLT/VISIR at a spatial resolution of 0.5 arcsec to probe the $6 \text{ arcsec} \times 6 \text{ arcsec}$ surroundings of Antares in the Q1 filter at $17.7 \mu\text{m}$. They identify six dusty clumps (at distances ranging from 40–96 R_{\star}), as well as unresolved emission from the innermost region – i.e. the region that is probed here in more detail. Assuming

¹<https://www.eso.org/public/news/eso2003/>

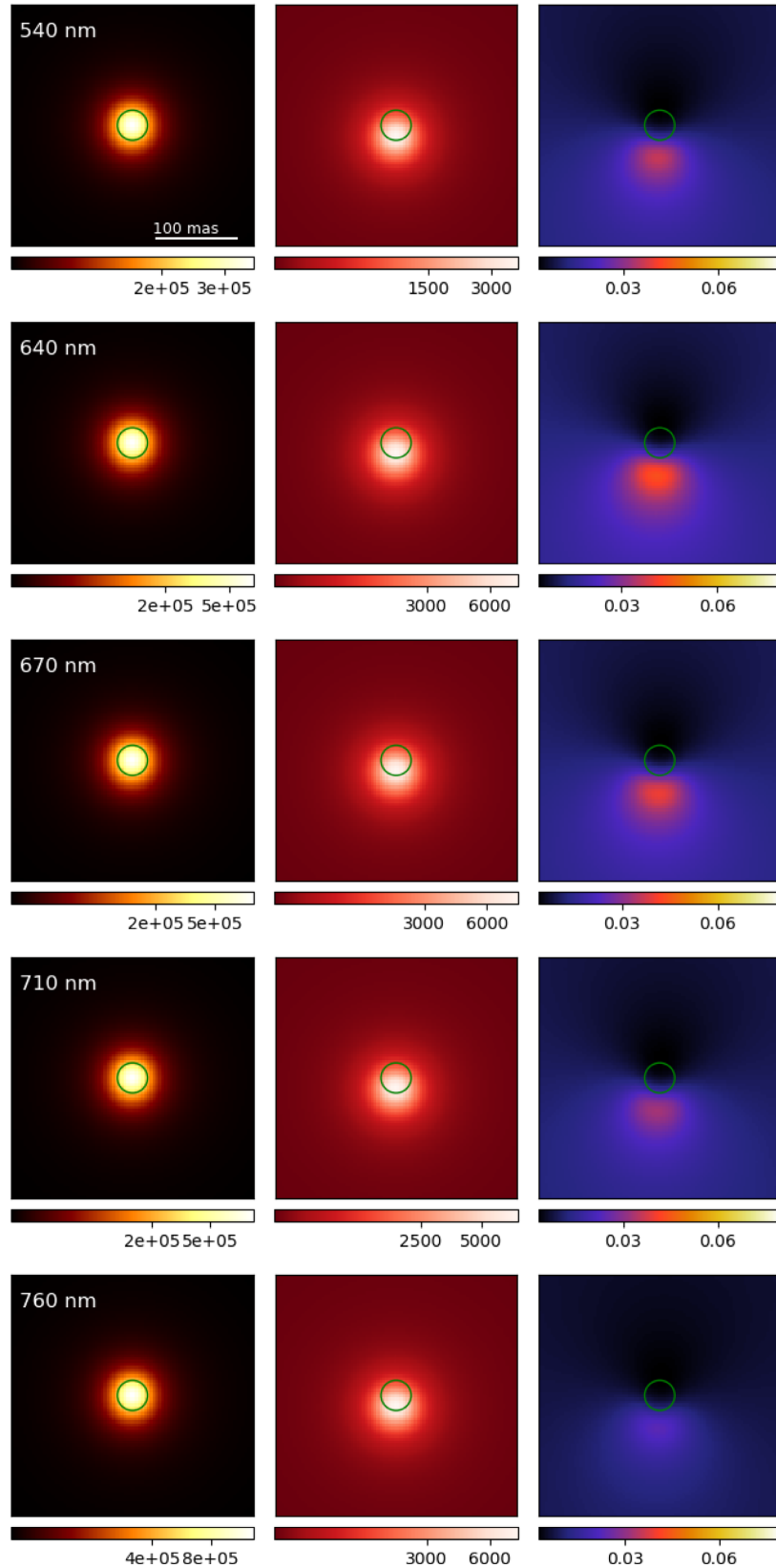


Figure 6. Best matched MCMAX3D model as determined by comparison of the DoLP to the observations. First column: Intensity images ($\text{W m}^{-2} \mu\text{m}^{-1} \text{sr}^{-1}$). The green circle indicates the size of the photosphere. Second column: Polarized flux ($\text{W m}^{-2} \mu\text{m}^{-1} \text{sr}^{-1}$). Third column: DoLP.

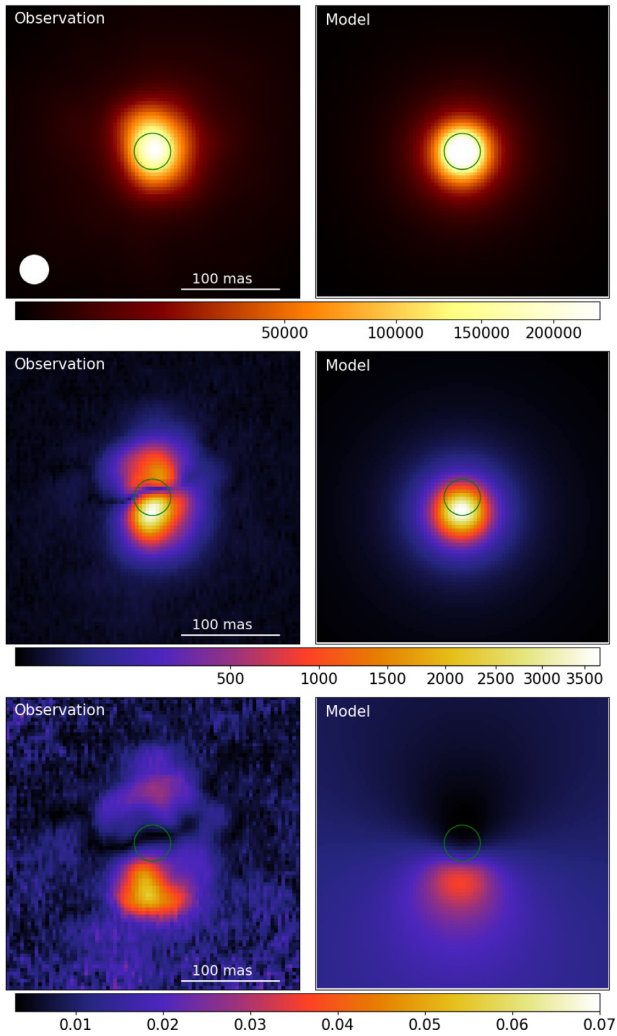


Figure 7. Comparison of observations (left) to the models (right) in the V filter. First row: Intensity images ($\text{W m}^{-2} \mu\text{m}^{-1} \text{sr}^{-1}$). The green circle indicates the size of the photosphere. Second row: Polarized flux ($\text{W m}^{-2} \mu\text{m}^{-1} \text{sr}^{-1}$). Third row: DoLP.

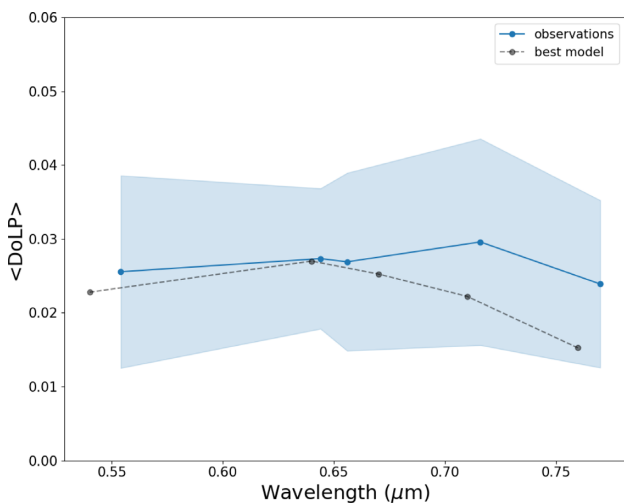


Figure 8. The average DoLP within the southern clump of our best-fitting model (see Table 3) as a function of wavelength. Blue circles and blue homogeneous background denote the observations and their uncertainties.

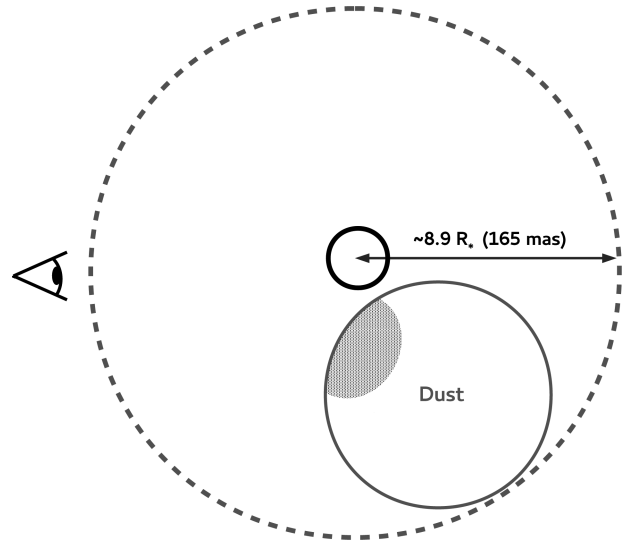


Figure 9. Schematic showing the dust clump and star relative to the direction towards the observer. The furthest edge of the clump from the star is at 165 mas or $8.9 R_*$, corresponding to a dynamical flow time from Antares of about 4 yr assuming a radial wind speed of 34 km s^{-1} . Only part of the clump (approximated by the shaded area) is prominently visible in polarized light. See text for a discussion.

the dust consists of an astronomical silicate mixture (Draine & Li 2007), they find typical dust masses of their resolved clumps of $(3\text{--}6) \times 10^{-9} M_{\odot}$, hence total clump masses of $(0.6\text{--}1.2) \times 10^{-6} M_{\odot}$ adopting $\psi = 200$. These values are similar to the total mass we derive for the near-surface clump that is scrutinized here.

The clumps studied by Ohnaka (2014) are spatially unresolved or only marginally resolved, therefore we cannot directly compare clump sizes. Assuming all clumps have a similar size when ejected by the star, the VISIR image implies that internal expansion may have increased their radii by at most a factor of a few. By comparing to an earlier image of Antares' nearby environment by Marsh et al. (2001), taken with the MIRLIN focal-plane array camera at Keck II, Ohnaka (2014) estimates the clumps to move out with projected velocities of $13\text{--}40 \text{ km s}^{-1}$ which the authors conclude is not consistent with a simple monotonically accelerating outflow.

5.3 Modes and potential driving mechanisms of mass-loss from Antares

Braun et al. (2012) combine measurements of notably Zn II absorption line strengths in the line of sight towards the companion Antares B and hydrodynamical simulations of the way in which the B2.5 V star creates density perturbations in a radial wind from Antares, as well as an H II region, to derive the mass-loss in gas. They find $\dot{M} = (2.0 \pm 0.5) \times 10^{-6} M_{\odot} \text{ yr}^{-1}$.

How does this total mass-loss rate compare to a mean mass-loss in ejected dusty clumps? Ohnaka (2014, see Section 5.2) estimated that the six clumps they observed around Antares to have a mean projected outward directed dusty clump velocity of 34 km s^{-1} , implying a dynamical crossing time of the projected zone from the closest observed clump to the star to the most distant ($40\text{--}96 R_*$) of 24.7 yr. This yields a typical clump ejection time-scale of $\sim 5 \text{ yr}$ and a mean mass-loss rate in clumps of approximately $1.5 \times 10^{-7} M_{\odot} \text{ yr}^{-1}$ adopting $\psi = 200$. However, this is a lower limit to the clump mass-loss as it relies on a velocity estimation based on the clump motion

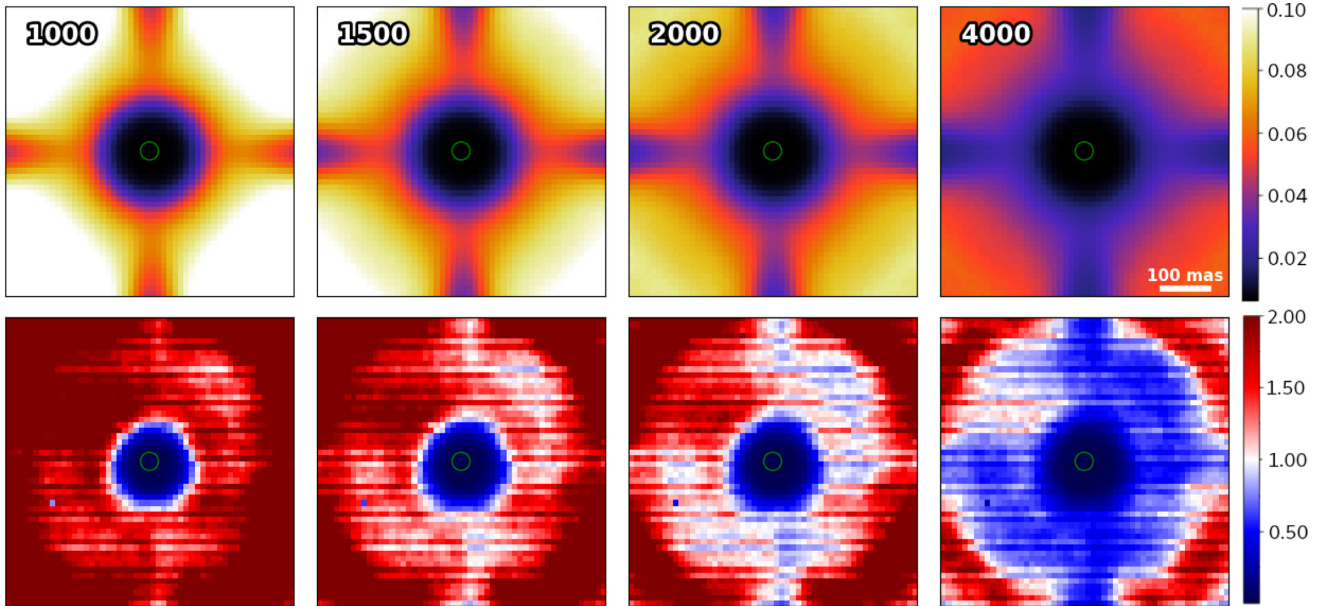


Figure 10. Models of the DoLP produced for a dusty radial outflow in the V-filter. The mass-loss rate is set at $2 \times 10^{-6} M_{\odot} \text{ yr}^{-1}$ and the terminal flow velocity at 30 km s^{-1} . Dust condensation is assumed to start at $5 R_{*}$. From left to right, the gas-to-dust ratio is 1000, 1500, 2000, and 4000. Top panels show the predicted DoLP in the model. Bottom panels show the predicted DoLP divided by the RMS map of the observations. Blue indicates a less than 1σ detection; red a detection that is above 1σ . As we do not detect significant polarization in the region outside of the clump, this yields a lower limit to the gas-to-dust ratio of the radial outflow in this region of $\psi_{\min} = 2000$.

in the VISIR field of view. The latter captures only the displacement in the plane of the sky and neglects the motion in the line of sight. Consequently, the actual velocity of each clump could be higher leading to a larger mass-loss rate. Additionally, the adopted gas-to-dust ratio of 200 is highly uncertain which would significantly affect our calculation of the total mass lost through clumps.

The clump in this study had likely not yet been ejected at the time of Ohnaka’s 2010 observations, however, its dust mass is comparable to those of the outer clumps studied by Ohnaka (2014). Taken at face value, the findings of Ohnaka and the present results suggest that the mass-loss in ejected clumps contributes significantly to the total mass-loss. To provide insight on whether it represents the main mass-loss mechanism or is one of more contributors would require further knowledge of the 3D kinematics of the dusty clumps.

At present, we may only speculate as to the mechanism ejecting clumps of material from the surface of Antares. Variability in both light and radial velocity reveals two preferred characteristic time-scales for the star, one of 100–350 d and one of about 6 yr (e.g. Stothers 2010; Pugh & Gray 2013a, b). The former has been associated with the typical lifetime of convective cells at the surface (e.g. Chiavassa et al. 2011) and with fundamental mode or first-order overtone pulsations (e.g. Stothers 1969). The latter may be connected to stochastic oscillations (e.g. Kiss, Szabó & Bedding 2006), or to the turnover time of convective motions (Stothers 2010). The typical time-scale for clump ejection seems to agree best with the latter, longer time-scale. 3D hydrodynamical simulations show that the surface of RSG stars is covered by a few large convective cells only (e.g. Chiavassa & Freytag 2015) with time-scales dependent on the size and depth of the cell (Schwarzschild 1975). If gas would be released over the full extent of such a cell – provided conditions were right – the surface covering factor would be in line with the 18 per cent derived for the clump that is studied here. Given that

not each and every surfacing convective cell releases a cloud of gas, suitable conditions for launching material may depend on the interplay of the multiple processes, likely including convection and pulsations.

Does dust also form in the (initially) radial outflow from Antares as e.g. probed and modelled by Braun et al. (2012)? The top four panels of Fig. 10 show predictions of the DoLP for a radial flow from the star with a mass-loss rate of $2 \times 10^{-6} M_{\odot} \text{ yr}^{-1}$ and a terminal velocity of 30 km s^{-1} . The gas-to-dust ratio is set to $\psi = 1000, 1500, 2000,$ and 4000 (gas-to-dust ratios below these values show a clear detection in the SPHERE images), and silicate dust is assumed to form instantaneously at $5 R_{*}$. Silicate dust is chosen for the outflow as we expect the lower temperature at this distance to allow for the condensation of less temperature sensitive dust species. The bottom panels show the DoLP predicted by these models divided by the RMS map of the observations. The models were run for the V-filter as it has the lowest uncertainties (being the widest of the six filters used). In these bottom plots, the blue areas correspond to where the detection is below 1σ and the red areas are above 1σ . We conclude that the minimum gas-to-dust ratio is $\psi_{\min} \sim 2000$ given this mass-loss rate, as otherwise we would have detected a polarized signal at the 1σ level.

These results clearly point to at most partial dust formation in the radially streaming wind from the star. Dust nucleation computations by Boulanger et al. (2019) indicate a critical density $n_{\text{H}} \sim 5 \times 10^{10} \text{ g cm}^{-3}$ for dust nucleation to set in a galactic environment. This is about three orders of magnitudes larger than the density at $5 R_{*}$ in Antares’s flow of $2 \times 10^{-6} M_{\odot} \text{ yr}^{-1}$, and may help explain the high value for the lower limit ψ_{\min} that we report here. Höfner et al. (2016) constrain the minimum density of dust grains in AGB outflows for a dust-driven outflow to develop at $n_{\text{d}} \geq 4 \times 10^{-6} \text{ cm}^{-3}$. For a population of $0.1 \mu\text{m}$ silicate grains, this converts to a maximum gas-to-dust ratio for dust driving to occur of $\psi_{\text{max-dd}} \sim 500$. Given their

higher luminosities, this value may be somewhat higher for RSGs. Still, the derived ψ_{\min} and estimated $\psi_{\max\text{-dd}}$ seem to suggest that the amount of solid state material that may actually form in the radial outflow from Antares is too little to efficiently power a dust-driven wind. If so, the radial outflow requires an altogether different driving mechanism. However, it should be noted that our observations and models here can only account for the inner wind (as pictured in Fig. 10) and may not be representative of what is happening further out from the star. Modelling of *ISO-SWS* spectra of Antares by Justtanont et al. (1999) also gives a high minimum gas-to-dust ratio in the wind of 600. Dust driving may then only be relevant for the episodic ejection of clumps of gas, in which apparently dust is condensing efficiently, possibly because associated shocks and turbulent eddies produce significant small-scale overdensities.

5.4 Comparison to other RSGs

Antares is not the only RSG that has shown evidence for a more inhomogeneous wind. The few RSGs of which the circumstellar environment has been studied show a wide range of characteristics possibly connected to their evolutionary stage. The RSG VY CMa has shown extreme episodic mass-loss (Sciicluna et al. 2015; Kamiński 2019). A study by Kamiński (2019) using ALMA has shown a dusty envelope containing several large clumps. Modelling of the observations suggests that it is these clumps – being episodically expelled into the interstellar medium – that are responsible for the high mass-loss (instead of being a result of a steady spherical wind). NOEMA observations of the CO $J = 2-1$ line (Montargès et al. 2019) of the RSG μ Cep also suggest that the ejection of clumps from the circumstellar environment is a large contributor (≥ 25 per cent) to the mass-loss. SPHERE/ZIMPOL observations of Betelgeuse (Kervella et al. 2016) also show a patchy and clumpy inner circumstellar environment and a departure from spherical symmetry in the visible. The clumpy nature of the environment of Betelgeuse has also been observed out to tens of stellar radii with VLT/VISIR by Kervella et al. (2011). A study of the variations of the silicate feature by comparison of IRAS LRS spectra and other ground-based spectra of RSGs spanning 25 yr by Monnier, Geballe & Danchi (1999) shows that the mass-loss characteristics and dust signatures can vary over both short and long time-scales. Multiple modes of mass-loss, i.e. a clumpy and dusty episodic mass-loss and a dust-poor radial outflow of gas, therefore is likely a general phenomenon among RSGs. Which of these modes is dominant may depend on stellar properties and surface conditions.

6 SUMMARY AND CONCLUSIONS

The SPHERE/ZIMPOL observations of Antares show a strong localized signal in the DoLP which indicates the presence of a large dusty clump in the inner circumstellar environment. Modelling the observations using the radiative transfer code MCMAX3D shows that the clump is $2.6\text{--}4.4 R_{\star}$ in size with a dust mass of about $(0.3\text{--}1.5) \times 10^{-8} M_{\odot}$. Our models place the edge of the clump beyond the plane of the sky through the centre of Antares (so, the dusty clump is ‘behind’ the star) and its inner edge within $0.5 R_{\star}$ from the stellar surface. Adopting full condensation of solids in the dusty clumps ($\psi \sim 200$) and incorporating findings by Ohnaka (2014), we find a minimum mass-loss rate from clumps of $1.5 \times 10^{-7} M_{\odot} \text{ yr}^{-1}$. No significant polarization is measured in the rest of the probed ambient environment, placing constraints on the abundance of dust in a radially streaming stellar wind. Using the canonical value for this radial mass-loss of $2 \times 10^{-6} M_{\odot} \text{ yr}^{-1}$ (Braun et al. 2012), the

gas-to-dust ratio in this flow must be at least $\psi_{\min} = 2000$ in the field of view of ZIMPOL. This suggests that the inner region of the radial flow is not dust driven.

The surface covering factor of the dusty clump (18 per cent) agrees quite well with the expected size of surfacing convective cells in RSGs. Moreover, the estimated typical ejection time-scale for clumps (of ~ 5 yr; Ohnaka 2014) matches well with a characteristic time-scale for photometric and radial velocity variability (of ~ 6 yr) that has been associated with (an interplay of) pulsational and convective behaviours. This points towards convection and pulsation playing a role in the launching mechanism of the dusty clumps. The methodology developed here, i.e. to constrain the 3D position of recently ejected dusty-clumps, in principle allows to empirically study a possible connection of this mode of mass-loss with surface activity. This requires long-term simultaneous interferometric monitoring of surface structures and the direct stellar surroundings. Supplementing this with kinematic information through resolved spectroscopy may further aid in establishing or rejecting such a connection.

ACKNOWLEDGEMENTS

The authors acknowledge funding from the KU Leuven C1 grant MAESTRO C16/17/007. This project has received funding from the European Union’s Horizon 2020 research and innovation program under the Marie Skłodowska-Curie Grant agreement no. 665501 with the research Foundation Flanders (FWO) ([PEGASUS]² Marie Curie fellowship 12U2717N awarded to MM). LD acknowledges support from the ERC consolidator grant 646758 AEROSOL. This work has made use of the SPHERE Data Centre, jointly operated by OSUG/IPAG (Grenoble), PYTHEAS/LAM/CESAM (Marseille), OCA/Lagrange (Nice), Observatoire de Paris/LESIA (Paris), and Observatoire de Lyon. We acknowledge with thanks the variable star observations from the AAVSO International Database contributed by observers worldwide and used in this research. This research made use of IPYTHON (Pérez & Granger 2007), NUMPY (van der Walt, Colbert & Varoquaux 2011), MATPLOTLIB (Hunter 2007), SCIPY (Virtanen et al. 2020), ASTROPY,² a community-developed core PYTHON package for Astronomy (Astropy Collaboration 2013), and UNCERTAINTIES³: a PYTHON package for calculations with uncertainties.

Based on observations made with ESO Telescopes at the La Silla Paranal Observatory under programme ID 095.D-0458.

DATA AVAILABILITY

The data underlying this article are available from the ESO archive under programme ID 095.D-0458.

REFERENCES

- Abdul-Masih M. et al., 2019, *ApJ*, 880, 115
 Airapetian V. S., Ofman L., Robinson R. D., Carpenter K., Davila J., 2000, *ApJ*, 528, 965
 Aronson E., Bladh S., Höfner S., 2017, *A&A*, 603, A116
 Asplund M., Grevesse N., Sauval A. J., Scott P., 2009, *ARA&A*, 47, 481
 Astropy Collaboration, 2013, *A&A*, 558, A33
 Beasor E. R., Davies B., 2016, *MNRAS*, 463, 1269
 Begemann B., Dorschner J., Henning T., Mutschke H., Gürtler J., Kömpe C., Nass R., 1997, *ApJ*, 476, 199

²Available at <http://www.astropy.org/>

³Available at <http://pythonhosted.org/uncertainties/>

- Bennett P. D., 2010, in Leitherer C., Bennett P. D., Morris P. W., Van Loon J. T., eds, ASP Conf. Ser. Vol. 425, Hot and Cool: Bridging Gaps in Massive Star Evolution. Astron. Soc. Pac., San Francisco, p. 181
- Beuzit J. L. et al., 2019, *A&A*, 631, A155
- Bohren C. F., Huffman D. R., 1998, Absorption and Scattering of Light by Small Particles. Wiley, New York
- Boulangier J., Gobrecht D., Decin L., de Koter A., Yates J., 2019, *MNRAS*, 489, 4890
- Braun K., Baade R., Reimers D., Hagen H. J., 2012, *A&A*, 546, A3
- Cardelli J. A., Clayton G. C., Mathis J. S., 1989, *ApJ*, 345, 245
- Castelli F., Kurucz R. L., 2003, in Piskunov N., Weiss W. W., Gray D. F., eds, Proc. IAU Symp. 210, Modelling of Stellar Atmospheres. Astron. Soc. Pac., San Francisco, p. A20
- Chiavassa A., Freytag B., 2015, in Kerschbaum F., Wing R. F., Hron J., eds, ASP Conf. Ser. Vol. 497, Why Galaxies Care about AGB Stars III: A Closer Look in Space and Time. Astron. Soc. Pac., San Francisco, p. 11
- Chiavassa A., Freytag B., Masseron T., Plez B., 2011, *A&A*, 535, A22
- Corbally C. J., 1984, *ApJS*, 55, 657
- De Beck E., Decin L., de Koter A., Justtanont K., Verhoelst T., Kemper F., Menten K. M., 2010, *A&A*, 523, A18
- Draine B. T., Li A., 2007, *ApJ*, 657, 810
- Ducati J. R., 2002, VizieR Online Data Catalog, II/237
- Ekström S. et al., 2012, *A&A*, 537, A146
- Freudling W., Romaniello M., Bramich D. M., Ballester P., Forchi V., García-Dabó C. E., Moehler S., Neeser M. J., 2013, *A&A*, 559, A96
- Georgy C., 2012, *A&A*, 538, L8
- Gray R. O., Corbally C. J., Garrison R. F., McFadden M. T., Bubar E. J., McGahee C. E., O'Donoghue A. A., Knox E. R., 2006, *AJ*, 132, 161
- Harper G. M., Brown A., Lim J., 2001, *ApJ*, 551, 1073
- Hartmann L., Avrett E. H., 1984, *ApJ*, 284, 238
- Höfner S., 2008, *A&A*, 491, L1
- Höfner S., Freytag B., 2019, *A&A*, 623, A158
- Höfner S., Bladh S., Aringer B., Ahuja R., 2016, *A&A*, 594, A108
- Hunter J. D., 2007, *Comput. Sci. Eng.*, 9, 90
- Josselin E., Plez B., 2007, *A&A*, 469, 671
- Justtanont K., Tielens A. G. G. M., de Jong T., Cami J., Waters L. B. F. M., Yamamura I., 1999, *A&A*, 345, 605
- Kamiński T., 2019, *A&A*, 627, A114
- Kervella P., Perrin G., Chiavassa A., Ridgway S. T., Cami J., Haubois X., Verhoelst T., 2011, *A&A*, 531, A117
- Kervella P. et al., 2015, *A&A*, 578, A77
- Kervella P. et al., 2016, *A&A*, 585, A28
- Kiss L. L., Szabó G. M., Bedding T. R., 2006, *MNRAS*, 372, 1721
- Kochanek C. S., Khan R., Dai X., 2012, *ApJ*, 759, 20
- Koike C., Kaito C., Yamamoto T., Shibai H., Kimura S., Suto H., 1995, *Icarus*, 114, 203
- Levesque E. M., Massey P., 2020, *ApJ*, 891, L37
- Lucy L. B., 1974, *AJ*, 79, 745
- McWilliam A., 1990, *ApJS*, 74, 1075
- Marsh K. A., Bloemhof E. E., Koerner D. W., Ressler M. E., 2001, *ApJ*, 548, 861
- Mathis J. S., Rimpl W., Nordsieck K. H., 1977, *ApJ*, 217, 425
- Mauron N., Josselin E., 2011, *A&A*, 526, A156
- Min M. J., Hovenier J. W., Waters L. B. F. M., de Koter A., 2004, Book of abstracts of conference "Light, Dust and Chemical Evolution", Gerace, Italy, p. 28
- Min M., Hovenier J. W., de Koter A., 2005, *A&A*, 432, 909
- Min M., Dullemond C. P., Dominik C., de Koter A., Hovenier J. W., 2009, *A&A*, 497, 155
- Monnier J. D., Geballe T. R., Danchi W. C., 1999, *ApJ*, 521, 261
- Montargès M., Chiavassa A., Kervella P., Ridgway S. T., Perrin G., Le Bouquin J.-B., Lacour S., 2017, *A&A*, 605, A108
- Montargès M. et al., 2019, *MNRAS*, 485, 2417
- O'Gorman E. et al., 2020, *A&A*, 638, A65
- Ohnaka K., 2014, *A&A*, 568, A17
- Ohnaka K., Hofmann K.-H., Schertl D., Weigelt G., Baffa C., Chelli A., Petrov R., Robbe-Dubois S., 2013, *A&A*, 555, A24
- Ohnaka K., Weigelt G., Hofmann K. H., 2017, *Nature*, 548, 310
- Pérez F., Granger B. E., 2007, *Comput. Sci. Eng.*, 9, 21
- Pugh T., Gray D. F., 2013a, *AJ*, 145, 38
- Pugh T., Gray D. F., 2013b, *ApJ*, 777, 10
- Reimers D., Hagen H. J., Baade R., Braun K., 2008, *A&A*, 491, 229
- Richichi A., Lisi F., 1990, *A&A*, 230, 355
- Richichi A., Percheron I., Davis J., 2009, *MNRAS*, 399, 399
- Schmid H. M. et al., 2018, *A&A*, 619, A9
- Schwarzschild M., 1975, *ApJ*, 195, 137
- Scicluna P., Siebenmorgen R., Wesson R., Blommaert J. A. D. L., Kasper M., Voshchinnikov N. V., Wolf S., 2015, *A&A*, 584, L10
- Smartt S. J., 2009, *ARA&A*, 47, 63
- Snow, Theodore P. J., Buss, Richard H. J., Gilra D. P., Swings J. P., 1987, *ApJ*, 321, 921
- Stothers R., 1969, *ApJ*, 156, 641
- Stothers R. B., 2010, *ApJ*, 725, 1170
- Tielens A. G. G. M., 1990, in Mennessier M. O., Omont A., eds, From Miras to Planetary Nebulae: Which Path for Stellar Evolution?. Editions Frontières, Gif-sur-Yvette, p. 186
- Tramper F., Sana H., de Koter A., Kaper L., 2011, *ApJ*, 741, L8
- Tuthill P. G., Haniff C. A., Baldwin J. E., 1997, *MNRAS*, 285, 529
- van der Walt S., Colbert S. C., Varoquaux G., 2011, *Comput. Sci. Eng.*, 13, 22
- van Leeuwen F., 2007, *A&A*, 474, 653
- van Loon J. T., 2006, in Lamers H. J. G. L. M., Langer N., Nugis T., Annuk K., eds, ASP Conf. Ser. Vol. 353, Stellar Evolution at Low Metallicity: Mass Loss, Explosions, Cosmology. Astron. Soc. Pac., San Francisco, p. 211
- van Loon J. T., Zijlstra A. A., Bujarrabal V., Nyman L. Å., 2001, *A&A*, 368, 950
- Verhoelst T., van der Zypen N., Hony S., Decin L., Cami J., Eriksson K., 2009, *A&A*, 498, 127
- Virtanen P. et al., 2020, *Nat. Methods*, 17, 261
- Zubko V. G., Laor A., 2000, *ApJS*, 128, 245

APPENDIX:

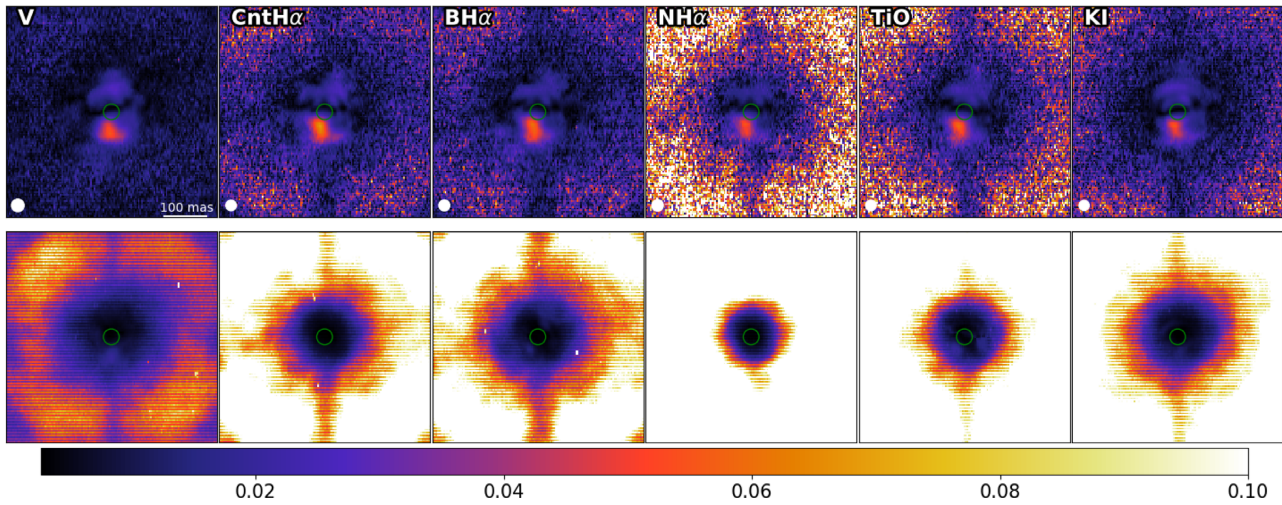


Figure A1. DoLP (top) with corresponding RMS map (bottom). Outside of the region of interest discussed in this study, the observations become dominated by noise.

This paper has been typeset from a $\text{\TeX}/\text{\LaTeX}$ file prepared by the author.